Advances in Geo-Energy Research

Vol. 20, No. 1, p. 1-15, 2026

Original article

Thermodynamics-based thermo-hydro-mechanical coupling model for sediment sand erosion and migration induced by hydrate depressurization dissociation

Rui Zhou[1], Yang Liu[1]*, Guangchang Yang[1], Wenhao Huang[2]

[1]*Department of Civil Engineering, University of Science and Technology Beijing, Beijing 100083, P. R. China*
[2]*INSA Rouen Normandie, Normandie University, Rouen F-76000, France*

Keywords:
Sand erosion and migration
thermo-hydro-mechanical coupling
thermodynamic theory
hydrate-bearing sediment
numerical modeling

Cited as:
Zhou, R., Liu, Y., Yang, G., Huang, W. Thermodynamics-based thermo-hydro-mechanical coupling model for sediment sand erosion and migration induced by hydrate depressurization dissociation. Advances in Geo-Energy Research, 2026, 20(1): 1-15.
https://doi.org/10.46690/ager.2026.04.01

Abstract:
The multi-field coupling mechanism between hydrate dissociation and sand production is a pivotal factor controlling hydrate exploitation efficiency. To elucidate the sand erosion and migration processes induced by hydrate dissociation, this study proposes a thermodynamics-based thermo-hydro-mechanical coupling model. This mechanical model considers the effects of deviator stress, seepage and hydrate saturation on sand erosion, and employs the critical migration rate concept to characterize the transition between sand migration and deposition. Besides, it incorporates porosity evolution induced by sand erosion, as well as the degradation of cementation stress. Gas-liquid seepage rate and sand migration rate are deduced using migration coefficient relationships. The model is verified through numerical simulations of hydrate dissociation experiments with and without considering sand production. The proposed theoretical model can describe the nonlinear evolution law of sand erosion and migration induced by hydrate dissociation advancement, along with variations in temperature and axial displacement. Moreover, it is established that hydrate saturation exerts a more remarkable promotive effect on both gas production and sand production than depressurization pressure.

1. Introduction

Natural gas hydrate is widely recognized as a promising clean energy resource with significant development potential, therefore its safe and efficient extraction has recently become a major research focus (Li et al., 2025). However, a high proportion of 83% of sediment particles in the hydrate reservoir of the Shenhu area are smaller than 40 μm (Zhou et al., 2017). Hydrate dissociation induced by depressurization leads to pore enlargement and a reduction in cementation stress (Ning et al., 2022). Under external loading, the soil skeleton reorganizes and sand particles are driven by gas and liquid phase seepage. This involves multiple processes, such as migration, deposition, further migration, and pore blockage (Sibille et al., 2015; Kazidenov et al., 2025). Elucidating the dynamic evolution of sand erosion and the migration process during hydrate dissociation is essential for improving the production efficiency and developing effective sand control strategies.

Hydrate dissociation and deviator stress are key factors controlling sand erosion (Li et al., 2024). Liquid seepage is the dominant factor in sand migration (Oyama et al., 2010; Murphy et al., 2020). Besides, sand erosion tests conducted under different loading conditions indicate that the stress level influences sand migration by modifying the cementation state between particles (Cohen et al., 2019; Zhang et al., 2025). Experimental research indicates that sand production is gov-

Yandy Scientific Press

*Corresponding author.
E-mail address: ruizhou@ustb.edu.cn (R. Zhou); yangliu@ustb.edu.cn (Y. Liu); yang3ang@ustb.edu.cn (G. Yang); wenhao.huang@insa-rouen.fr (W. Huang).

Received December 23, 2025; revised January 22, 2026; accepted February 17, 2026; available online February 20, 2026.

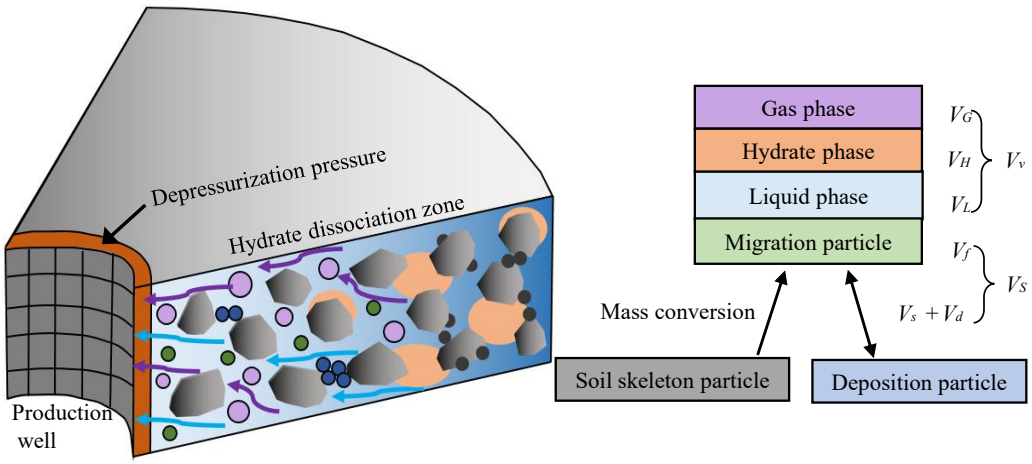

Fig. 1. Erosion and migration of solid particles induced by hydrate dissociation (Wang et al., 2023).

erned more by hydrate saturation rather than by the stress level (Fang et al., 2021). However, these studies primarily focused on the total amount of sand produced, lacking quantitative analysis of the dynamic processes of sand erosion, migration and deposition, as well as the coupling mechanisms among sand migration and hydrate dissociation.

Developing thermo-hydro-mechanical (THM) coupling models is essential to accurately capture the coupling mechanism between sand migration and hydrate dissociation. The most commonly used criterion for sand migration is the critical hydraulic gradient (Akaki and Kimoto, 2020; Uchida et al., 2022). To simplify model calculations, many studies have further adopted critical liquid seepage velocity as the erosion criterion and established empirical relationships linked to hydrate saturation (Yang et al., 2019; Zhu et al., 2020). Furthermore, sand erosion models based on theoretical methods, such as using equivalent plastic strain, stress balance and discrete element method simulation, have been successfully applied (Fujisawa et al., 2010; Wood et al., 2010; Katagiri et al., 2017). This approach inevitably neglects the coupling among multiple physical fields, particularly with respect to the effects of sand erosion on porosity (Yoneda et al., 2015; Li et al., 2024; Dou et al., 2025). However, the thermodynamic-based THM coupling modeling approach offers a novel solution to these challenges (Bai et al., 2023, 2024). As for the sand production process, the energy dissipation associated with sand migration at the microscale still needs to be formulated (Zhou et al., 2024).

This paper first incorporates the gas-liquid seepage velocity and sand migration rate into the dissipative force system. Then, by introducing the concept of granular temperature, the transfer relationship between mesoscale and macroscopic energy dissipation is established. Finally, the theoretical unification of sand production and THM coupling dissociation of hydrate based on granular thermodynamic theory is achieved. Hydrate dissociation is simulated with and without considering the sand migration process. The model is verified through gas production volume, sand production mass, and axial displacement.

2. THM coupling model for hydrate dissociation and sand production

2.1 Basic principles of the granular thermodynamic theory

2.1.1 Assumptions

Natural gas hydrate under external loading consists of solid (S), liquid (L), gas (G), and hydrate phases (H) (Zhu et al., 2020). During hydrate dissociation and gas/liquid migration, the solid particle can be eroded, causing the migration of soil particles. Therefore, the solid phase can be represented as the soil skeleton particle (s), the migration particle (f), and the deposition particle (d) (Fig. 1).

The following assumptions are set:

1) mass transfer between the skeleton and deposition particles is neglected (Uchida et al., 2022);
2) free water is assumed not to convert with bound water;
3) liquid water is pure, containing no dissolved methane gas;
4) the effects of temperature on liquid density and viscosity are assumed to be negligible;
5) considering that the temperature reductions induced by hydrate dissociation are limited, the ice phase is not taken into account, so as to simplify the model.

2.1.2 Granular thermodynamic theory

The granular thermodynamic theory provides a unified framework to account for energy dissipation during mechanical deformation, heat conduction, seepage, and hydrate dissociation (Bai et al., 2023). Existing studies provide a rational explanation of classical gas-liquid seepage and heat conduction. This study further introduces mesoscopic energy dissipation associated with sand migration (granular entropy Ω_g). By incorporating this mechanism into the overall energy dissipation framework through the concept of granular temperature, the model achieves a theoretical unification of hydrate dissociation and sand production (Fig. 2).

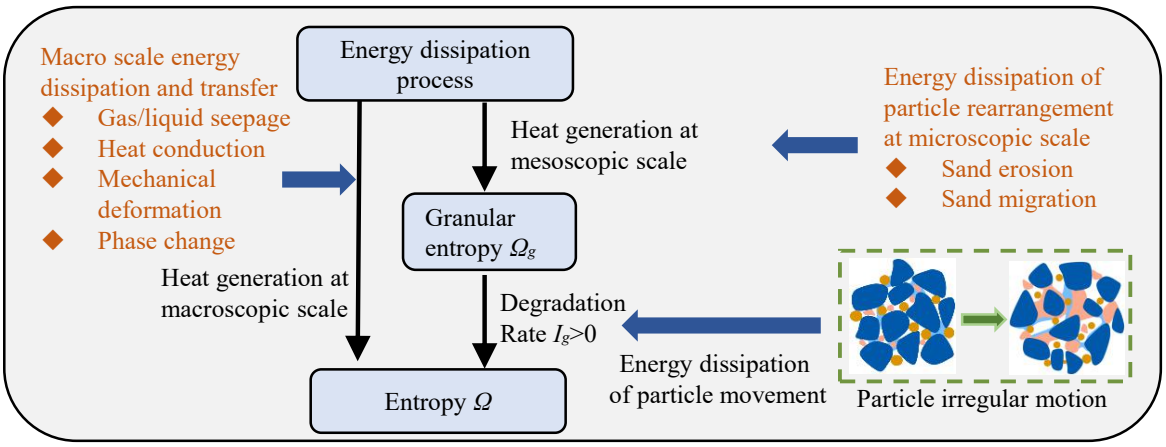

Fig. 2. Energy dissipation of hydrate-bearing sediment at the macroscopic and mesoscopic scales.

2.1.3 Conservation equations

On the basis of the material composition of hydrate-bearing sediment (Fig. 1), the mass conservation equation for each phase is formulated using the superposition principle:

$$\frac{\partial}{\partial t}\rho^{\alpha}+\nabla_k\rho^{\alpha}v_k^{\alpha}=m^{\alpha}\quad(\alpha=\mathrm{L,G,H}) \tag{1}$$

where ρ^{α}, v_k^{α} and m^{α} represent the density fraction, velocity and mass exchange rate of each phase, respectively.

The solid particle phase is further refined, and the mass conservation equations are formulated for the soil skeleton particles (s), migration particles (f), and deposition particles (d), such as:

$$\frac{\partial}{\partial t}\left(\rho^{s}\right)+\nabla_k\left(\rho^{s}v_k^{s}\right)=-m^{s} \tag{2}$$

$$\frac{\partial}{\partial t}\left(\rho^{d}\right)+\nabla_k\left(\rho^{d}v_k^{d}\right)=m^{fd}-m^{df} \tag{3}$$

$$\frac{\partial}{\partial t}\left(\rho^{f}\right)-D\nabla^2\left(\rho^{f}\right)+\nabla_k\left(\rho^{f}v_k^{f}\right)=m^{s}-m^{fd}+m^{df} \tag{4}$$

where m^{fd} represents the mass exchange from migration particles to deposition particles; m^{df} represents the mass exchange from deposition particles to migration particles; D represents the migration sand diffusion coefficient; m^{s} represents the mass exchange of solid particles.

The momentum, energy and entropy capacity conservation equations are established by referring to Bai et al. (2023):

$$\begin{aligned}&\frac{\mathrm{d}}{\mathrm{d}t}\left(\sum_{\alpha=\mathrm{s,f,d,L,G,H}}\rho^{\alpha}v_i^{\alpha}\right)+\sum_{\alpha=\mathrm{s,f,d,L,G,H}}\nabla_j\sigma_{ij}^{\alpha}\\&+\sum_{\alpha=\mathrm{f,L,G}}\rho^{\alpha}\left(v_i^{\alpha}-v_i^{s}\right)=\sum_{\alpha=\mathrm{s,f,d,L,G,H}}\rho^{\alpha}g_i\end{aligned} \tag{5}$$

$$\begin{aligned}&\sum_{\alpha=\mathrm{s,f,d,L,G,H}}\rho^{\alpha}\mathrm{d}_t e_{\alpha}=\sum_{\alpha=\mathrm{s,f,d,L,G,H}}\sigma_{jk}^{\alpha}\psi_{jk}^{\alpha}+\nabla_k\left(\varpi_k\right)\\&-\sum_{\alpha=\mathrm{f,L,G}}v_k^{\alpha}\left(\nabla_k\sigma_{ii}^{\alpha}+\rho^{\alpha}\nabla_k e_{\alpha}\right)+H\end{aligned} \tag{6}$$

$$\begin{aligned}&\sum_{\alpha=\mathrm{s,f,d,L,G,H}}\rho^{\alpha}\frac{\mathrm{d}\vartheta_{\alpha}}{\mathrm{d}t}=\\&\frac{R_a}{T}+\nabla_k f_k-\sum_{\alpha=\mathrm{f,L,G}}\rho^{\alpha}\left(v_i^{\alpha}-v_i^{s}\right)\nabla_k\vartheta_{\alpha}\end{aligned} \tag{7}$$

where σ_{ij}^{α}, e_{α}, ψ_{ij}^{α}, ϑ_{α} respectively denote the stress tensor, specific energy, deformation rate and entropy capacity of each phase; R_a represents the heat generation at macroscopic scale; H represents the dissipated energy of hydrate dissociation; ϖ_k represents the energy dissipation of heat conduction; v_i^{s} represents the movement rate of solid phase; T denotes the temperature; f_k is the heat conduction at macroscopic level.

To characterize sand erosion and migration, the granular temperature T_g and granular entropy are introduced. The conservation equation of granular entropy is expressed by referring to Eq. (7):

$$\rho^{s}\frac{\mathrm{d}\vartheta_g}{\mathrm{d}t}=\frac{R_g}{T_g}-I_g \tag{8}$$

where R_g denotes the mesoscopic heat generation; I_g is the entropy attenuation rate.

2.1.4 Thermodynamic differential equations

In porous media, the material-independent state variables and their conjugates can be represented as $\{\rho^{\alpha},M_i^{\alpha},\mathrm{d}\varepsilon_{ij}^{e},\Omega,\Omega_g\}$ and $\{\tau^{\alpha},v_i^{\alpha},\pi_{ij},T,T_g\}$, respectively. The total energy differential equation is then obtained by multiplying the state variables by their corresponding state conjugates:

$$\begin{aligned}&\mathrm{d}w=\sum_{\alpha=\mathrm{s,f,d,L,G,H}}\left(\tau^{\alpha}\mathrm{d}\rho^{\alpha}+v_i^{\alpha}\mathrm{d}M_i^{\alpha}\right)+\pi_{ij}\mathrm{d}e_{ij}^{e}+\\&T_g\mathrm{d}\Omega_g+T\mathrm{d}\Omega\end{aligned} \tag{9}$$

where τ^{α} and M_i^{α} represent the chemical potential and momentum of each phase; π_{ij} denotes the particle contact force; ε_{ij}^{e} is the elastic strain; Ω and Ω_g are the entropy and granular entropy, respectively.

Eq. (9) is simplified using the specific energy e, incorporating the mass (Eqs. (1)-(4)), momentum (Eq. (5)), energy (Eq. (6)), and entropy conservation equations (Eqs. (7) and (8)).

Finally, the thermodynamic differential relationship expressed in terms of energy dissipation $(R_a+R_g)_1$ is established as follows:

$$\begin{aligned}(R_a+R_g)_1=&\sum_{\alpha=\mathrm{s,f,d,L,G,H}}\psi_{ij}^{\alpha}\sigma_{ij}^{\alpha}-\sum_{\alpha=\mathrm{f,L,G}}\left[v_k^{\alpha}\left(\nabla_k\sigma_{ii}^{\alpha}+\rho^{\alpha}\nabla_k e_{\alpha}\right)+T\rho^{\alpha}v_k^{\alpha S}\nabla_k\vartheta_{\alpha}\right]-\rho^s\tau^s\left(\rho^s\psi_{kk}^s-m^s\right)\\&-\rho^d\tau^d\left(\rho^d\psi_{kk}^d+m^{fd}-m^{df}\right)-\rho^f\tau^f\left(\rho^f\psi_{kk}^f+D\nabla^2\rho^f-v_k^{fS}\nabla_k\rho^f+m^s-m^{fd}+m^{df}\right)\\&-\rho^L\tau^L\left(\rho^L\psi_{kk}^L-v_k^{LS}\nabla_k\rho^L+m^L\right)-\rho^H\tau^H\left(\rho^H\psi_{kk}^H-m^H\right)-\rho^G\tau^G\left(\rho^G\psi_{kk}^G-v_k^{GS}\nabla_k\rho^G+m^G\right)\\&+H+\nabla_k\left(\varpi_k-f_kT\right)+\pi_{ij}\mathrm{d}c_{ij}^p-\pi_{ij}\mathrm{d}\psi_{ij}^s+T_gI_g+f_k\nabla_kT\end{aligned}\tag{10}$$

The total energy dissipation of the dissociation system is formulated as the product of dissipative forces and dissipative flows. The macroscale dissipative forces, representing the source terms driving the system away from equilibrium, can be expressed as $\{\pi_{ij},T_g,\nabla_kT,\psi_{ij}^S,\psi_{ij}^H,\psi_{ij}^L,\psi_{ij}^G,v_i^{LS},v_i^{GS},v_i^{fS}\}$. The corresponding dissipative flows, describing the incremental responses to these forces, are expressed as $\{Y_{ij},I_g,q_k,\sigma_{ij}^{vS},\sigma_{ij}^{vH},\sigma_{ij}^{vL},\sigma_{ij}^{vG},\chi^{LS},\chi^{GS},\chi^{fS}\}$.

Regarding the dissipative force components at the mesoscale, in addition to the mesoscale contact force σ_{ij}^{vg}, hydrate saturation rate, and suction change rate described in Bai et al. (2023), the effects of the hydrate decomposition rate d_tS_H and the volume concentration of migration particles C_f should also be considered. Accordingly, the overall energy dissipation relationship between the macroscale and mesoscale can be expressed as $(R_a+R_g)_2$:

$$\begin{aligned}(R_a+R_g)_2=&\pi_{ij}Y_{ij}+I_gT_g+\sum_{\alpha=\mathrm{s,f,d,L,G,H}}\sigma_{ij}^{v\alpha}\psi_{ij}^{\alpha}\\&+\sum_{\beta=\mathrm{f,L,G}}\chi_k^{\beta S}v_k^{\beta S}+q_k\nabla_kT+\sigma_{ij}^{vg}\psi_{ij}^S+\Re T_g\mathrm{d}_tS_H\\&+\Delta H\cdot R_H+sT_g\mathrm{d}_tS_e+f\left(\mathrm{d}_tC_f,v_f\right)\end{aligned}\tag{11}$$

where R_H represents the hydrate dissociation rate per molar mass; ΔH represents the dissociation energy per molar mass; q_k represents the dissipative flow of temperature gradient; s and S_e represent the suction stress and effective saturation, respectively; S_H denotes the hydrate saturation; C_f and v_f denote the volume concentration and velocity of migration particles, respectively.

The energy dissipation $(R_a+R_g)_1$ is equal to the energy dissipation $(R_a+R_g)_2$. By comparing the corresponding terms in Eqs. (10) and (11), the following can be inferred:

$$Y_{ij}=\mathrm{d}_t\varepsilon_{ij}^p\tag{12}$$

$$f_k=q_k\tag{13}$$

$$\nabla_k\left(\varpi_k-f_kT\right)=0\tag{14}$$

$$\Delta H\cdot R_H=H\tag{15}$$

$$\chi_i^{\alpha S}=\rho^{\alpha}\tau^{\alpha}\nabla_k\rho^{\alpha}-\nabla_k\sigma_{ii}^{\alpha}-\rho^{\alpha}\nabla_ke_{\alpha}+T\rho^{\alpha}\nabla_k\vartheta_{\alpha}\quad(\alpha=\mathrm{L,G,f})\tag{16}$$

$$-\rho^f\tau^fD\nabla^2\rho^f=f\left(\mathrm{d}_tC_f,v_f\right)\tag{17}$$

$$\begin{aligned}&-\Re T_g\mathrm{d}_tS_H-sT_g\mathrm{d}_tS_e+n_H\rho_H\tau^Hm^H\\&-n_L\rho_L\tau^Lm^L-n_G\rho_G\tau^Gm^G=0\end{aligned}\tag{18}$$

Eqs. (12)-(18) provide dynamic inferences within the framework of granular thermodynamics, considering hydrate dissociation and sand migration.

2.2 THM coupling dissociation model

2.2.1 Temperature conservation equation

Bai et al. (2024) established the relationship between specific energy e and specific heat Γ (Eq. (19)). Thus, the following expression of Eq. (6) is obtained:

$$\sum_{\alpha=\mathrm{s,f,d,L,G,H}}\rho^{\alpha}\mathrm{d}_te_{\alpha}=\sum_{\alpha=\mathrm{s,f,d,L,G,H}}\rho^{\alpha}\Gamma_{\alpha}\mathrm{d}_tT\tag{19}$$

$$\sum_{\alpha=\mathrm{f,L,G}}v_k^{\alpha S}\rho^{\alpha}\nabla_ke_{\alpha}=v_k^{\alpha S}\rho^{\alpha}\Gamma_{\alpha}\nabla_kT\tag{20}$$

where Γ_α and $v_k^{\alpha S}$ represent the specific heat and relative velocity of each phase.

The dissipative force q_k and ϖ_k can be expressed as (Bai et al., 2024):

$$q_k=\frac{1}{T}\kappa_T\nabla_kT+\theta^Lv_k^{LS}+\theta^Gv_k^{GS}\tag{21}$$

$$\nabla_k\left(\varpi_k\right)=\nabla_k\left(\kappa_T\nabla_kT\right)+\nabla_k\left[\theta^Lv_k^{LS}T+\theta^Gv_k^{GS}T\right]\tag{22}$$

where κ_T denotes the heat conduction coefficient; θ^β denotes the migration coefficient of velocity (β=L,G).

Combining Eqs. (6) and (19)-(22), the temperature conservation equation for hydrate dissociation is established:

$$\sum_{\alpha=\mathrm{s,f,d,L,G,H}}\left(\rho^{\alpha}\Gamma_{\alpha}\mathrm{d}_tT-\sigma_{jk}^{\alpha}\psi_{jk}^{\alpha}\right)=\nabla_k\left(\kappa_T\nabla_kT\right)+\nabla_k\left[\theta^Lv_k^{LS}T+\theta^Gv_k^{GS}T\right]-\sum_{\alpha=\mathrm{f,L,G}}v_k^{\alpha S}\left(\nabla_k\sigma_{ii}^{\alpha}+\rho^{\alpha}\Gamma_{\alpha}\nabla_kT\right)+H\tag{23}$$

where H represents the energy transfer caused by the hydrate dissociation, which can be calculated by Eq. (15); ΔH is represented as E_1+E_2T (Akaki and Kimoto, 2020).

2.2.2 Gas and liquid seepage model

On the basis of the relationship between the migration coefficients (Zhou et al., 2024), the relationships between the dissipative forces $(v_k^L-v_k^S)$, $(v_k^G-v_k^S)$ and the dissipative flows χ_k^L, χ_k^G are established, considering the influence of the temperature gradient:

$$\chi_k^{\beta}=\theta^{\beta}\nabla_kT+\gamma^{\beta}\left(v_k^{\beta}-v_k^S\right)\quad(\beta=\mathrm{L,G})\tag{24}$$

$$\chi_k^f=\theta^f\nabla_kT+\gamma^f\left(v_k^f-v_k^S\right)\tag{25}$$

By further combining Eqs. (6), (24) and (25), the following simplified expression can be obtained:

$$\nabla_k e_\beta = T\nabla_k \vartheta_\beta + \tau^\beta \nabla_k \rho^\beta \quad (\beta = \mathrm{L,G,f}) \tag{26}$$

$$\gamma^\beta v_k^{\beta S} = -\nabla_k P_\beta - \theta^\beta \nabla_k T \quad (\beta = \mathrm{L,G,f}) \tag{27}$$

where γ^β represents the migration coefficient of each phase; P_β is the pore pressure of each phase.

According to Bai et al. (2023), the migration coefficients γ^L and γ^G are expressed as parameters related to the permeability coefficient of hydrate-bearing sediment: $\gamma^L = u_L/(K\cdot k_L)\delta_{ik}$, $\gamma^G = u_G/(K\cdot k_G)\delta_{ik}$, and $\gamma^f = \alpha_f u_L/(K\cdot k_L)\delta_{ik}$. Consequently, Eq. (27) can be simplified as follows:

$$v_i^{\beta S} = -\frac{Kk_\beta}{u_\beta}\nabla_i P_\beta - \frac{Kk_\beta}{u_\beta}\theta^\beta \nabla_i T \quad (\beta = \mathrm{L,G}) \tag{28}$$

$$v_i^{fS} = -\alpha_f \frac{Kk_\beta}{u_\beta}\nabla_i P_L \tag{29}$$

where K represents the reservoir permeability; k_β and u_β represent the relative permeability and viscosity coefficient of each phase, respectively; α_f is the migration sand velocity coefficient.

The natural convection of liquid and gas phases is expressed as $(K\cdot k_L)/u_L \times \nabla_i(P_L)$ and $(K\cdot k_G)/u_G \times \nabla_i(P_G)$ (Bai et al. (2023)). By substituting Eq. (28) into Eq. (1), the hydraulic field conservation equation is obtained:

$$\frac{\partial\left(nS_\beta\rho_\beta\right)}{\partial t} + \nabla\cdot\left[nS_\beta\rho_\beta\left(-\frac{Kk_\beta}{u_\beta}\nabla_k P_\beta - \frac{Kk_\beta}{u_\beta}\theta^\beta\nabla_k T\right)\right] + nS_\beta\rho_\beta \mathrm{d}_t\varepsilon_v = m^\beta \quad (\beta = \mathrm{L,G}) \tag{30}$$

where n stands for porosity; S_β denotes the saturation of each phase; ε_v is the volumetric strain.

The capillary pressure (P_c) can be expressed as a combination of effective saturation (S_e) and reference pressure P_0:

$$P_c = P_G - P_L = P_0\left[(S_e)^{-1/\chi} - 1\right]^{1-\chi} \tag{31}$$

$$S_e = \frac{S_L - S_{Lr}}{1 - S_H - S_{Gr} - S_{Lr}} \tag{32}$$

where χ denotes the model parameter; $S_{\beta r}$ is the residual saturation of each phase (β=L,G).

The relative permeability k_L and k_G can be expressed as:

$$k_L = S_e^{1/2}\left[1 - \left(1 - S_e^{1/\eta}\right)^\eta\right]^2 \tag{33}$$

$$k_G = (1 - S_e)^{1/2}\left(1 - S_e^{1/\eta}\right)^{2\eta} \tag{34}$$

where η denotes the parameter of relative permeability.

2.2.3 Stress and strain relationship

The stress-strain relationship of porous media employs the elastic potential energy density function to characterize the elastic-plastic deformation (Bai et al., 2023):

$$w_e = B\left[\frac{1}{k+2}(\varepsilon_v^e)^{k+2} + \xi(\varepsilon_v^e)^k(\varepsilon_e^e)^2\right] + \alpha_t(S_H)^{\beta_t}\exp(-\lambda_v\varepsilon_v^e - \lambda_s\varepsilon_s^e)\varepsilon_v^e + \frac{S_L P_L + S_G P_G}{S_L + S_G}\varepsilon_v^e \tag{35}$$

where k represents the elastic energy parameter; ε_v^e and ε_e^p represent the elastic and plastic strain, respectively; α_t, β_t, λ_v and λ_s are parameters related to cementation stress; B and ξ are the stiffness and friction parameters, respectively.

The contact stress π_{ij} corresponds to the effective stress σ_{ij} in classical elastoplastic mechanics (Bai et al. (2023)) and can be expressed as the differential of the elastic strain with respect to the potential energy density function:

$$\sigma_{ij} = B\left\{\left[(\varepsilon_v^e)^{k+1} + k\xi(\varepsilon_v^e)^{k-1}(\varepsilon_e^e)^2\right] + \alpha_t(S_H)^{\beta_t}\exp(-\lambda_v\varepsilon_v^e - \lambda_s\varepsilon_s^e) + \frac{S_L P_L + S_G P_G}{S_L + S_G}\right\}\delta_{ij} + 2\xi\xi_e^e(\varepsilon_v^e)^k \tag{36}$$

where e_{ij}^e denotes the deviator elastic stress.

The stiffness parameter B is described as $B = B_0 \times \exp(-n/\lambda(1-n))$, and the plastic strain rate is obtained by combining the migration coefficient η_{ijkl} with Eq. (36):

$$\mathrm{d}_t\varepsilon_{ij}^p = \left[(T_g)^\kappa\left(\frac{\eta_v}{3K_e} - \frac{\eta_s}{6G_e}\right)\delta_{ij}\delta_{kl} + (T_g)^\kappa\frac{\eta_s}{2G_e}\delta_{ik}\delta_{jl}\right]\pi_{ij} \tag{37}$$

where κ, η_v and η_s are the migration parameters; K_e denotes the elastic volumetric modulus ($K_e = B\left[(\varepsilon_v^e)^{k+1} + k\xi(\varepsilon_v^e)^{k-1}(\varepsilon_e^e)^2/\varepsilon_v^e\right]$); G_e is the elastic shear modulus ($G_e = B\xi(\varepsilon_v^e)^k$).

By combining Eqs. (36) and (37) and defining $T_{gg} = \eta_s(T_g)^\kappa$, the following expression is obtained:

$$\mathrm{d}_t\varepsilon_{ij}^p = C_1 T_{gg}\left[\varepsilon_v^e + \frac{\alpha_t(S_H)^{\beta_t}\exp(-\lambda_v\varepsilon_v^e - \lambda_s\varepsilon_s^e)}{K_e}\right]\delta_{ij} + T_{gg}e_{ij}^e \tag{38}$$

In Eq. (38), the granular temperature represents the macroscopic plastic deformation resulting from the microscopic particle rearrangement (Bai et al. (2023)). The conservation equation for granular temperature is formulated as:

$$\mathrm{d}_t T_{gg} = C_2 C_s\frac{\mathrm{d}_t e_{ij}\mathrm{d}_t e_{ij}}{\rho^s} + C_3 C_s\frac{\mathrm{d}_t\varepsilon_v\mathrm{d}_t\varepsilon_v}{\rho^s} + C_4\frac{\Re\mathrm{d}_t S_H + s\mathrm{d}_t S_e - \rho^f\tau^f D\nabla^2\rho^f}{\rho^s} - C_5\frac{T_{gg}}{\rho^s} \tag{39}$$

where C_1-C_5 are model parameters; e_{ij} denotes the deviator stress; ε_v is the volumetric strain.

2.2.4 Hydrate dissociation model

Referring to Kimoto et al. (2010), the hydrate phase change reaction equation is expressed as:

$$m^H = -k_d^0 M_H n S_H(P_e - P_G)\exp\left(\frac{-\Delta E_d}{R_H T}\right)\left[\frac{n^3(1-S_H)^3}{2K}\right]^{1/2} \tag{40}$$

where k_d^0 represents the intrinsic dissociation rate; M_α represents the molar mass of each phase; P_e denotes the phase change pressure; ΔE_d is the activation energy.

The hydrate dissociation model is established by combining the hydrate mass conservation equation (Eq. (1)) with Eq. (40), which can be derived as:

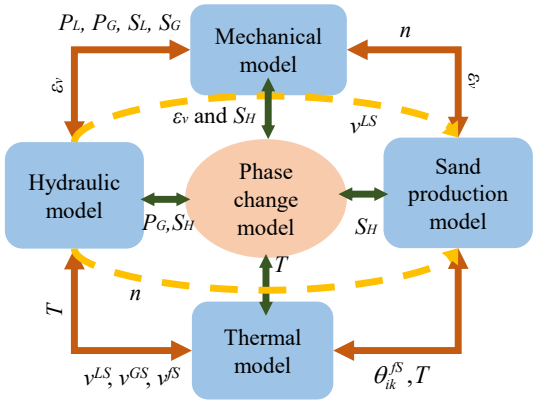

Fig. 3. Multi-field relationships within the THM coupling dissociation and the sand production model.

$$n\rho_L \mathrm{d}_t S_H = -k_d^0 M_H n S_H \left(P_e - P_G\right) \exp\left(\frac{-\Delta E_d}{R_H T}\right) \left[\frac{n^3 \left(1-S_H\right)^3}{2K}\right]^{1/2} - nS_H \rho_H \mathrm{d}_t \varepsilon_v \tag{41}$$

Zhang et al. (2025) expressed the permeability and hydrate phase change pressure P_e as follows:

$$P_e = \exp\left(\mathrm{e}_1 - \frac{\mathrm{e}_2}{T}\right) \tag{42}$$

$$K = K_0 \left(1 - S_H\right)^N \tag{43}$$

where e_1 and e_2 represent the phase change pressure parameters; K_0 and N represent the intrinsic reservoir permeability and degradation coefficient, respectively.

The mass conversion among the hydrate, liquid and gas phases can be derived from the reaction equation $CH_4 \cdot (H_2O)N_{Hyd} \rightarrow CH_4 + N_{Hyd} \cdot H_2O$. The mass change rate of the liquid and gas phases are given by $m^L = N_{Hyd} M_L / M_H \times m^H$ and $m^G = M_G / M_H \times m^H$, respectively.

2.3 Sand erosion and migration model

2.3.1 Sand erosion model

By converting the mass conservation equation of the skeleton particles (Eq. (2)) into a corresponding porosity expression and performing a further simplification step, the following relationship is obtained:

$$\frac{\mathrm{d}n}{\mathrm{d}t} = \mathrm{d}_t V_s - \frac{1}{V}\mathrm{d}_t V_d - \left(1 - n - \frac{V_d}{V}\right)\varepsilon_v \tag{44}$$

where V_α represents the volume of each phase (α = s, f, d); V is the total volume.

According to Uchida et al. (2022), the sand erosion rate is expressed as:

$$\mathrm{d}_t V_s = -V_s w_1 \left[w_2 e_{ij} + \ln\left(\frac{V_s}{V_{s0}}\right) + \mathrm{M}^d\right] H\left(\frac{v^{LS}}{v_c} - 1\right) \tag{45}$$

where w_1 and w_2 are the sand erosion parameters; M^d denotes the initial detachability potential.

The critical migration velocity v_c can be established as a function of hydrate saturation and initial critical velocity v_{c0} ($v_c = v_{c0}(1 - S_H)^{w_3}$). The liquid relative velocity is obtained from Eq. (28). This approach is well established in the literature (Zhu et al., 2020; Uchida et al., 2022).

2.3.2 Sand migration and deposition model

The volume concentration C_f ($C_f = m^f / \rho_s n S_L$) used to simplify Eq. (4), and the resulting expression is:

$$\frac{\partial}{\partial t}\left(nS_L C_f\right) - nS_L D\nabla^2\left(C_f\right) + v^{fS} nS_L \nabla_i C_f = \mathrm{d}_t V_s - \mathrm{d}_t V_{fd} + \mathrm{d}_t V_{df} \tag{46}$$

Zhu et al. (2020) indicated that the introduction of migration sand alters the viscosity coefficient of the liquid phase, and the mixed viscosity coefficient can be expressed as:

$$\mu_L = \mu_{L0}\left[1 - \frac{C_f}{C_{f0}} - 2\left(\frac{C_f}{C_{f0}}\right)^{1.3}\left(1 - \frac{C_f}{C_{f0}}\right)^4\right]^{-2.5} \tag{47}$$

where C_{f0} and μ_{L0} represent the critical migration sand concentration and the viscosity coefficient of pure liquid, respectively. C_{f0} is calculated to be 0.6 (Zhu et al., 2020).

A step function $H(\cdot)$ is employed to describe this migration-deposition-further migration process. The resulting sand deposition function can be expressed as:

$$\mathrm{d}_t V_{fd} - \mathrm{d}_t V_{df} = \mathrm{d}_t V_d = \lambda_f C_f v^{fS} - H\left(\frac{v^{LS}}{v_c} - 1\right) V_d \tag{48}$$

In Eq. (48), the first term on the right-hand side describes the blockage mechanism, while the second term corresponds to the volume of deposition particles converted into migration particles.

3. Multi-field coupling relationships and numerical calculation strategy

3.1 Analysis of coupling relationships

The proposed model comprises mechanical, thermal, hydraulic, phase change, and sand production modules. Specifically, the mechanical field is governed by Eqs. (36), (38) and (39), the thermal field is reflected by Eqs. (23) and (15), the hydraulic field is represented by Eqs. (30)-(34), Eqs. (41)-(43) represent the phase change model, and Eqs. (44)-(48) represent the sand production module.

The proposed model provides a more comprehensive representation of coupled mechanisms (Fig. 3):

1) the mechanical field model accounts for the influence of sand erosion (V_s) in addition to gas pressure, liquid pressure, and the saturations of liquid, gas and hydrate;
2) the hydraulic field model considers both temperature conduction and thermal driving effects induced by temperature gradients;
3) the thermal field model is coupled with the volume concentration of migration particles;
4) the deposition-further migration process is incorporated into the sand production model.

3.2 Methods of parameter calibration

The calibration of the stiffness parameter B_0 uses the isotropic compression-rebound curve, while λ represents the slope of the compression curve in the e-$\lg p'$ plane. C_1 is

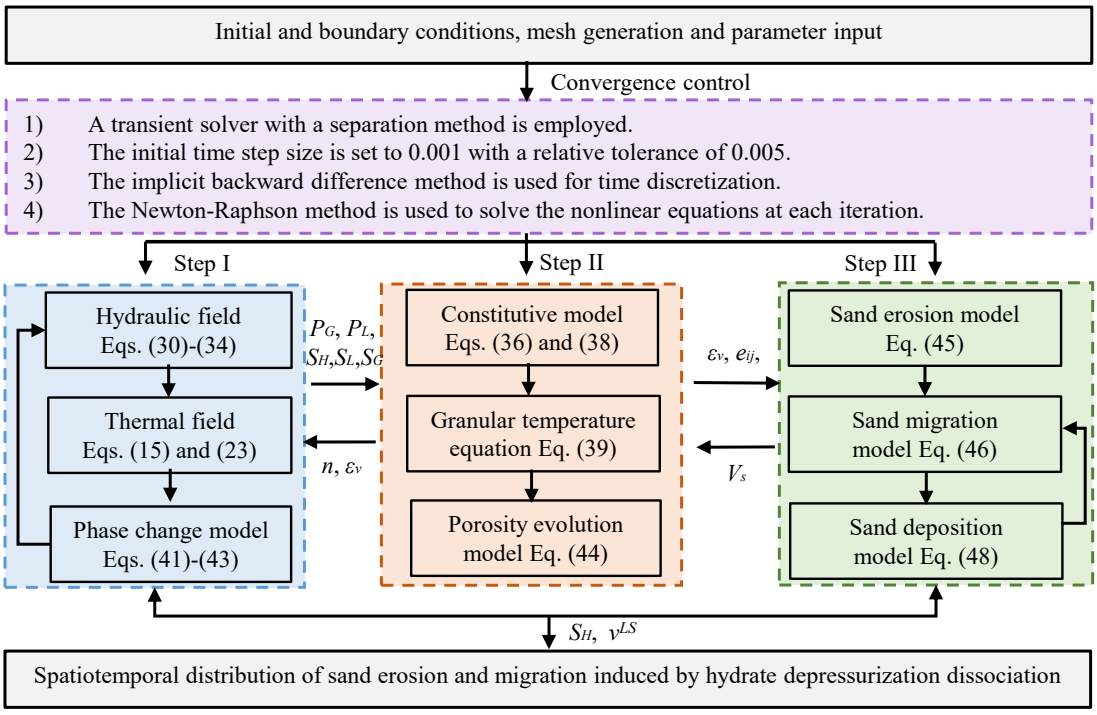

Fig. 4. Numerical calculation strategies and convergence control methods.

related to the specimen dilatancy ratio, and C_2 is calculated from the stress ratio when the drained shear of the hydrate sediment samples reaches the critical state (Bai et al. (2023)). C_3 is obtained by fitting the isotropic compression curve under $S_H = 0$, and C_4 is obtained by fitting the volumetric strain curve. C_5 is related to the stress relaxation of the sediment samples and is calibrated using the attenuation method described in Bai et al. (2023). The parameters α_t and β_t are determined by fitting the initial cementation stress curve using Eq. (36), with the initial cementation stress obtained by inverting the peak shear strength (Shen et al., 2016). Finally, λ_v and λ_s are simultaneously calculated based on the gas production volume and the displacement curve.

Referring to Uchida et al. (2022), the critical migration rate v_{c0} and w_3 are set as 0.01 m/d and 3, respectively. The parameter α_f is calibrated as $\alpha_f = C_f/(1-C_f)$ (Sun et al., 2023). The parameters w_1 and w_2 are fitted to match the sand production rate and sand production mass under different confining pressures. The parameter λ_f is calculated from the ratio of sand particle concentrations at the inlet and outlet (Cortis et al., 2006). M^d denotes the initial sand erosion rate, and V_{s0} is the initial sand particle volume, calculated by the initial porosity.

3.3 Modeling setup and convergence control

The displacement U, gas pressure P_G, liquid pressure P_L, temperature T, hydrate saturation S_H, volume of skeleton particles V_s, and migration sand concentration C_f are selected as basic variables. Modeling was performed using the finite software COMSOL Multiphysics 6.3, with the following setup:

1) the mechanical field model was implemented by the solid mechanics, PDE, and ODE modules;
2) the hydraulic, thermal, and phase change models were input via the PDE modules;
3) the sand erosion module was implemented using the ODE module;
4) the sand migration model was input using the PDE module.

The theoretical model was solved using a "separation" approach. First, the hydraulic, thermal and phase change modules were solved. Next, the mechanical field model was solved, followed by the sand production model (Fig. 4). Convergence control includes initial calculation compensation, selection of iterative methods, and determination of relative tolerances and time steps (Fig. 4).

4. Results and discussion

Bai et al. (2023) and Zhou et al. (2024) have validated the constitutive relations, gas-liquid seepage behavior, and heat conduction of the theoretical model. The prediction accuracy is evaluated using the mean squared error (MSE) and the coefficient of variation (COV), where a smaller MSE and COV indicate higher prediction accuracy. Tables 1 and 2 present the simulation parameter values and initial conditions, respectively, calculated by Lu et al. (2018) and Li et al. (2019, 2021).

4.1 Case I: Verification of hydrate dissociation

Referring to the dissociation steps in the experiment conducted by Li et al. (2019), three depressurization stages are simulated (Figs. 5(a) and 5(b)), named AB stage (3.6 ~ 6 MPa, $\Delta t = 20$ min), BC stage (6 MPa, $\Delta t = 40$ min), and CD stage

Table 1. Parameters used for hydrate dissociation and sand production simulation.

Mechanical model (Case I; Case II)		Hydrate dissociation and sand erosion model (Case II)			
Parameter	Value	Parameter	Value	Parameter	Value
B_0 (MPa)	6.03×10^7; 5.0×10^6	u_G (Pa·s)	1.01×10^{-3}	e_1; e_2	35.4; 9,459
k	0.5; 0.5	η	0.6	M_H (kg/mol)	0.124
λ	0.13; 0.13	S_{Lr}; S_{Gr}	0.1; 0.01	M_L; M_G (kg/mol)	0.018; 0.016
ξ	2.3; 5.0	R (J/mol/K)	8.31	k_d^0	1.25×10^{-5}
C_2	800; 800	N	5	ρ_S; ρ_H (kg/m^3)	2,150; 917
C_3 (s^2)	0.6; 0.28	ΔE_d	77,330	ρ_L; ρ_G (kg/m^3)	1,000; 0.684
C_4 (kg·m^{-3}·kPa^{-1})	0.03; 0.03	θ^L; θ^G (J/m^3/K^2)	8; 40	w_1 (h^{-1})	0.1
C_5 (kg·m^{-3}·s^{-1})	1×10^4; 1.8×10^4	Γ_S; Γ_H (J/kg/K)	750; 2,220	w_2; w_3	1; 3
α_t	1.67; 3.16	Γ_L; Γ_G	4,200; 2,180	D	2×10^{-4}
β_t	2.0; 1.84	κ_S; κ_H (W/m/K)	0.8; 0.3	v_{c0} (m/d)	0.01
λ_v	10; 6	κ_L; κ_G (W/m/K)	0.56; 0.03	λ_f	0.98
λ_s	6; 3	E_1	446,120	E_2	−132.6

Table 2. Initial and boundary conditions used for simulation.

Initial conditions	Case I	Case II
R (H) (mm)	25 (240)	63 (100)
P_{G0} (MPa)	13.5	11.0
S_{H0} (-)	0.25	0.47
n_0 (-)	0.46	0.3
S_{L0} (-)	0.65	0.43
K_0 (mD)	97.98	97.98
T_0 (K)	281.15	275.15

(3.8 ∼ 6 MPa, $\Delta t = 140$ min). The phase change pressure is calculated by Eq. (42), and the value of $P_e = 6$ MPa.

Both gas production and axial displacement exhibit a clear three-stage evolution characterized by slow growth, gradual stabilization and rapid development (Figs. 6(a) and 6(b)). The gas release during stage AB increases specimen porosity, leading to greater axial displacement under external load. As the dissociation reaction intensifies in stages BC and CD, the axial displacement transitions from a stable plateau to a rapid rise (Fig. 6(b)).

4.2 Case II: Sand production within the hydrate dissociation process

Referring to the experiment of Lu et al. (2018) (Fig. 7(a)), the simulated pressure is divided into three stages: AB, BC and CD (Fig. 7(b)). The corresponding phase change pressure is calculated to be 3.0 MPa by Eq. (42). Therefore, hydrate dissociation primarily occurs during stage BC, while stage CD represents the further release of gas and liquid after the dissociation reaction is complete.

4.2.1 Hydrate dissociation property

In the initial stage (AB), gas inside the specimen is discharged under the initial pressure gradient, resulting in a gas production of 6.5 L. As the pressure gradually drops below the phase transition pressure, hydrate dissociation begins, leading to a gas production of 44.5 L (Fig. 8(a)). Compared with simulations that do not consider sand production, gas production during the AE stage increases when sand erosion is included. In contrast, during the ED stage, the opposite trend emerges, indicating that migration particles gradually block pore channels.

It is worth noting that hydrate dissociation primarily occurs at the top and bottom of the critical extraction end and gradually propagates toward the central region (Fig. 8(b)). This phenomenon, as demonstrated by Fuente et al. (2019), is attributed to the endothermic nature of hydrate dissociation.

4.2.2 Deformation and heat transfer property

Axial displacement is the most pronounced during the BC stage, reaching 1.33 mm, while those in the AB and CD stages are 0.32 and 0.26 mm, respectively (Fig. 9(a)). Since hydrate dissociation is an endothermic process, the temperature boundary at the top of the hydrate layer exhibits asymmetry. Accordingly, the resulting temperature gradient facilitates the dissociation reaction (Fig. 9(b)).

4.2.3 Sand production mechanism

Deviator stress breaks the cementation between soil particles, causing sand particles to detach from the soil skeleton and be transported through pore channels with the liquid phase. The sample deformation further amplifies porosity changes. By the end of this stage ($t = 400$ min), the cumulative sand production reaches 0.85 g (Fig. 10).

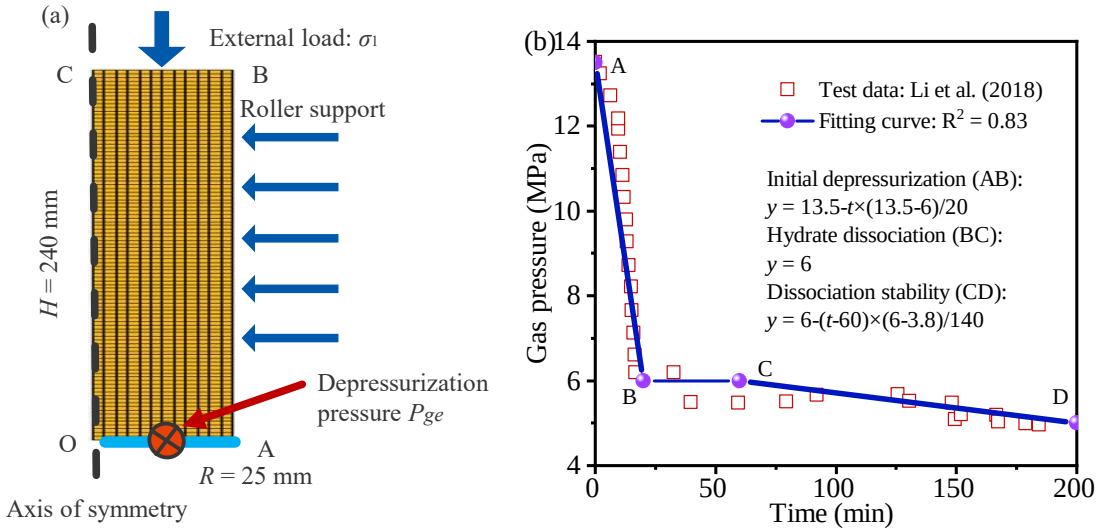

Fig. 5. Numerical modeling of hydrate dissociation experiment: (a) calculation model and (b) gas pressure.

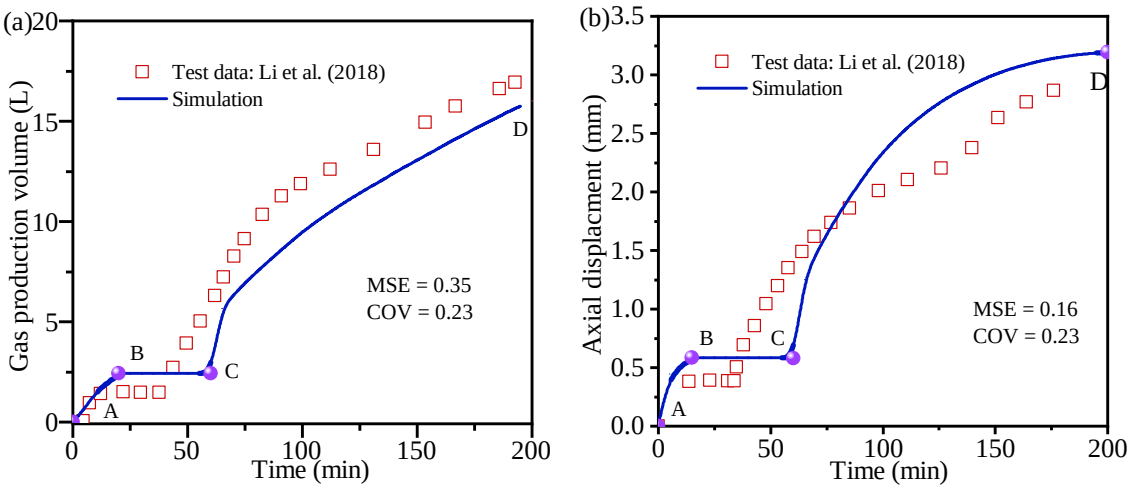

Fig. 6. Comparison between simulation and experimental values of hydrate dissociation: (a) Gas production volume and (b) axial displacement.

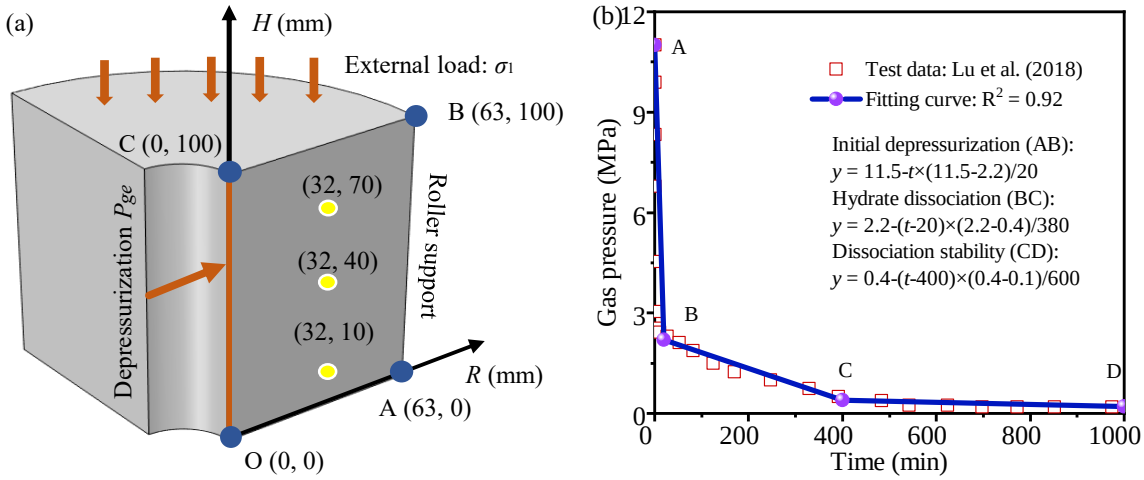

Fig. 7. Numerical modeling of hydrate dissociation and sand production experiment: (a) Calculation model and (b) gas pressure.

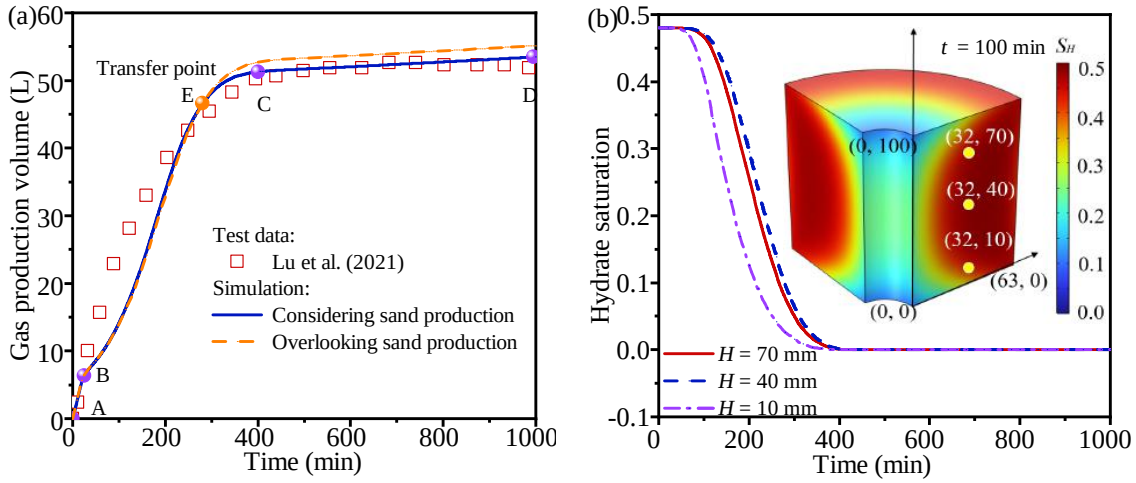

Fig. 8. Numerical simulation of hydrate dissociation experiment: (a) Gas production volume and (b) hydrate saturation.

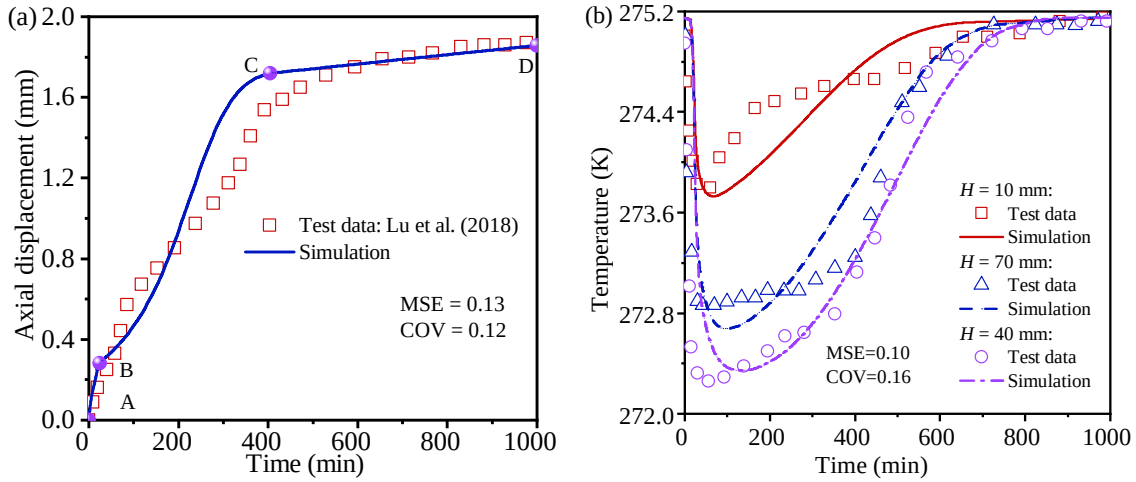

Fig. 9. Comparison between simulation and experimental values of hydrate dissociation: (a) Axial displacement and (b) temperature.

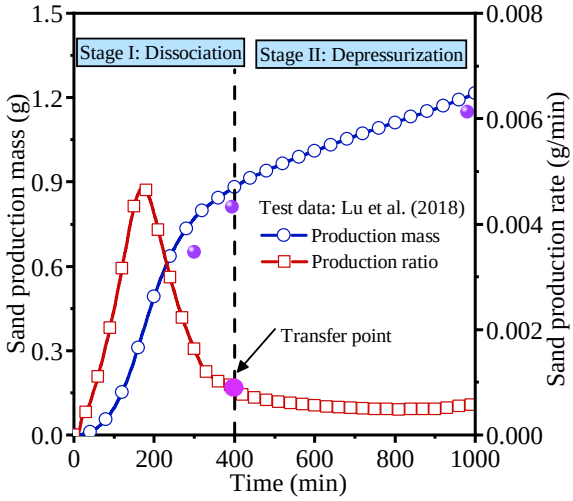

Fig. 10. Sand production rate and mass during the hydrate dissociation process.

Once the dissociation reaction is complete ($t = 400$ min), liquid water in the specimen is expelled from the depressurization end under the action of the pressure gradient. This effect induces the further migration of previously eroded particles. The sand production mass gradually increases between $t = 400 \sim 1{,}000$ min, and the total sand production reaches 1.21 g at $t = 1{,}000$ min (Fig. 10).

4.3 Sand erosion and migration

4.3.1 Sand erosion mechanism

The evolution curve of the sand erosion rate is illustrated in cross-sectional and longitudinal sections (cross-section: $H = 50$ mm; longitudinal section: $R = 18$ mm). As the hydrate dissociation reaction progresses, sand erosion initiates near the dissociation end and gradually expands inward over time (Fig. 11(a)). The sand erosion rate near the dissociation end shows an initial increase followed by stabilization over time, with the maximum sand erosion rate reaching 0.058 (Fig. 11(a)).

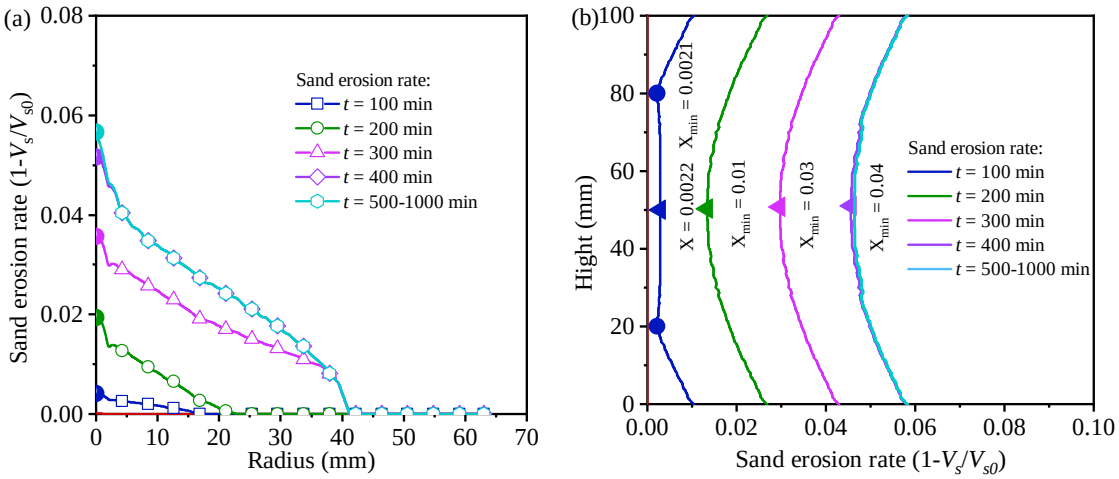

Fig. 11. Evolution of sand erosion rate during the hydrate dissociation process: (a): Cross-section area and (b) longitudinal section area.

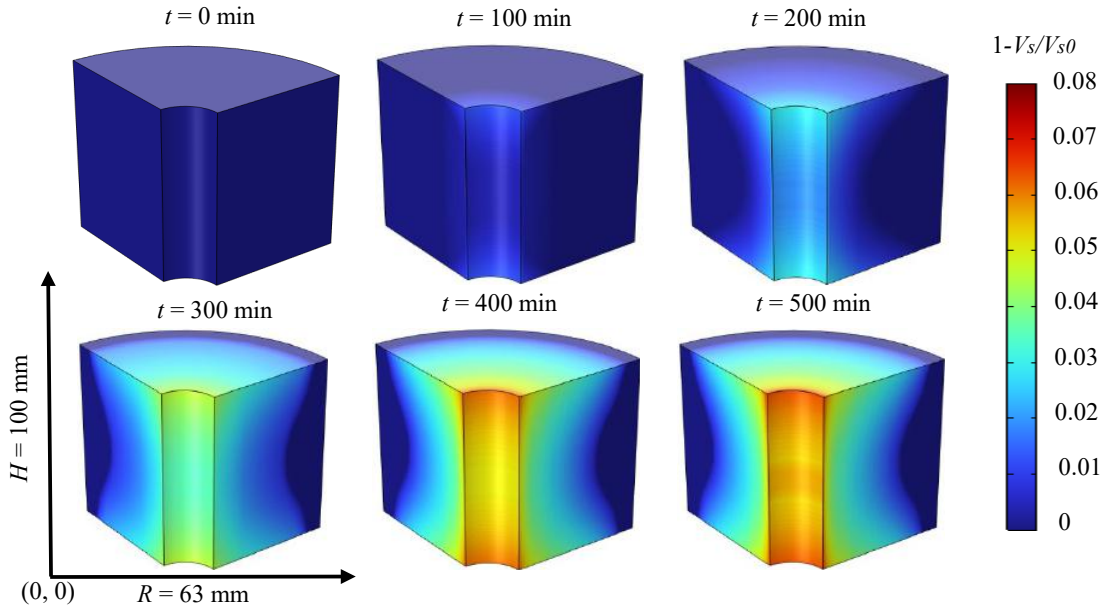

Fig. 12. Cloud diagram of sand erosion rate during the hydrate dissociation process.

During the period of $t = 0 \sim 100$ min, the sand erosion rate in the top and bottom regions is greater than that in the central region (Fig. 11(b)). The sand erosion rate initiates near the depressurization end and gradually develops toward the internal boundary regions (Fig. 12). Once hydrate dissociation is completed ($t > 500$ min), sand detachment tends to stabilize, indicating that the erosion process has reached a steady state.

4.3.2 Sand migration mechanism

From $t = 0 \sim 300$ min, the migration sand concentration (C_f) gradually increases, and the affected region expands outward to $R = 50$ mm (Fig. 13(a)). At $t = 500$ min, C_f reaches a maximum value of 0.088 near the dissociation end, while migration sand is generated at $R = 60$ mm with $C_f = 0.002$. Subsequently, as time progresses ($t = 500 \sim 1{,}000$ min), the C_f value near the dissociation end decreases.

The migration sand concentration (C_f) at the top and bottom regions is significantly higher than that in the middle region (Fig. 13(b)). The C_f values at (0, 50) and (0, 100) exhibit a pattern of initial increase followed by a decrease, with the turning point occurring at $t = 400$ min (Fig. 13(c)). Besides, the migration sand concentration (C_f) at point (63, 50) increases gradually throughout the process (Fig. 14).

5. Discussion of parameters

Hydrate saturation ($S_{H0} = 0.15, 0.30, 0.45$ and 0.6) and depressurization pressure ($P_{ge} = 0.1, 0.4, 1.0$ and 1.5 MPa) are key factors influencing sand erosion and migration. Other modeling parameters are same as the test of Lu et al. (2018) (Table 1). The ranges of hydrate saturation and depressurization pressure were selected based on the research of Li et al. (2019, 2024) and Ning et al. (2022). These ranges

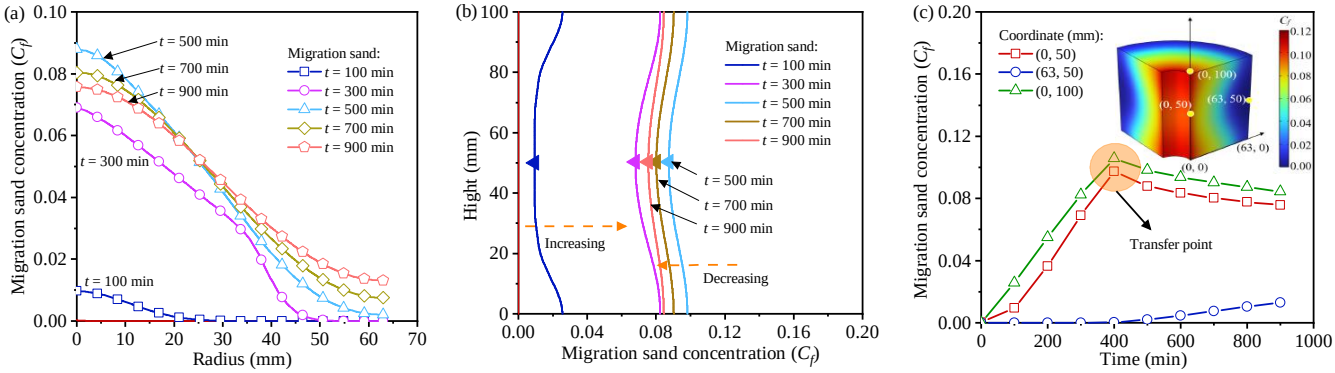

Fig. 13. Evolution of migration sand concentration during the hydrate dissociation process: (a) Cross-section area, (b) longitudinal section area, and (c) time effect.

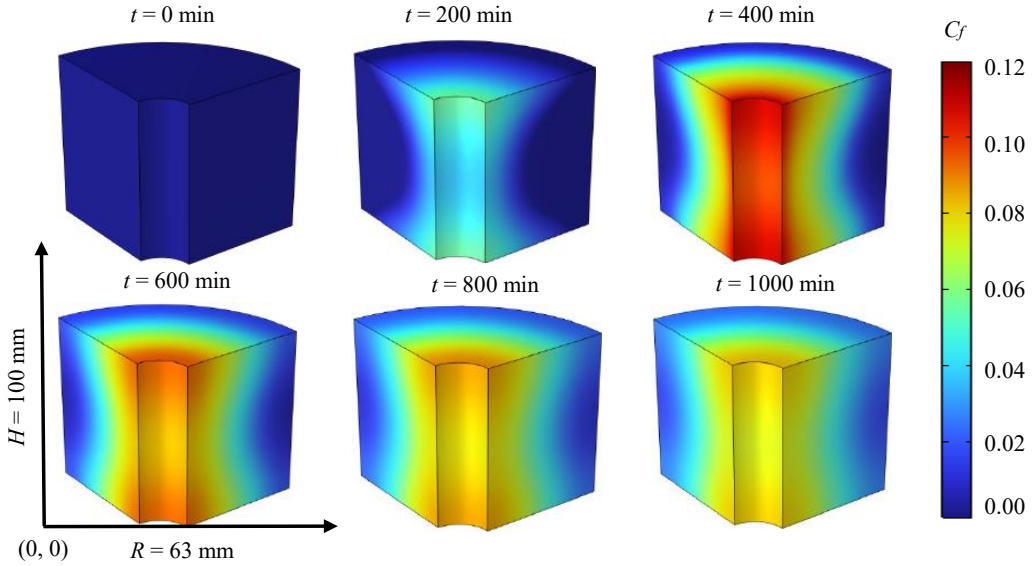

Fig. 14. Cloud diagram of migration sand concentration during the hydrate dissociation process.

encompass typical values observed in natural gas hydrate reservoirs.

5.1 Hydrate saturation effect

While higher hydrate saturation corresponds to greater total volumes of produced gas and sand (Figs. 15(a), 15(b)), the early-stage gas production rate is actually more pronounced under conditions of lower saturation. The initial gas production at $S_{H0} = 0.15$ reaches 23 L, accounting for 54.7% of the total gas production volume. In contrast, at $S_{H0} = 0.45$, the initial gas production is only 6.2 L. Notably, the initial sand production remains essentially unchanged across varying hydrate saturations ($t = 0 \sim 20$ min, Fig. 15(b)).

The sand erosion rate reaches its maximum at the depressurization end and decreases rapidly with the distance increasing. The erosion-affected range also expands with increasing hydrate saturation. When $S_{H0} = 0.6$, the erosion range extends to $R = 47$ mm, compared with only $R = 18$ mm at $S_{H0} = 0.15$. The region influenced by sand migration is larger than that for sand erosion (Figs. 16(a) and 16(b)).

5.2 Depressurization pressure effect

As the depressurization pressure decreases, the gas production volume in the BC section increases (Fig. 17(a)). However, the final gas production volume remains similar, all reaching approximately 51.5 L. Moreover, the depressurization pressure increases the liquid and gas phase flow rates (Eq. (28)), leading to an increase in the final sand production mass (Fig. 17(b)).

The sand erosion rate exhibits an overall increase due to the accelerated liquid seepage induced by depressurization pressure (Fig. 18(a)). In addition, the influence range of sand erosion expands as the depressurization pressure decreases. The migration sand concentration is positively correlated with depressurization pressure, and its influence range is larger than that of sand erosion (Fig. 18(b)).

6. Conclusions

This study establishes a THM coupling model for hydrate dissociation and sand production by integrating the gas-liquid seepage velocity and sand migration rate into the energy dissipation system based on a granular thermodynamic framework.

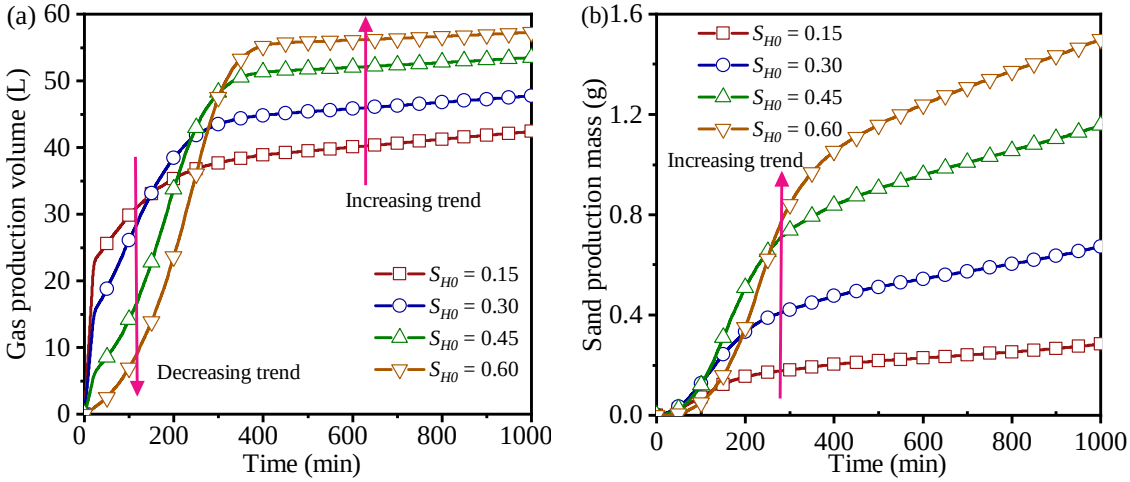

Fig. 15. Effect of hydrate saturation: (a) Gas production volume and (b) sand production mass.

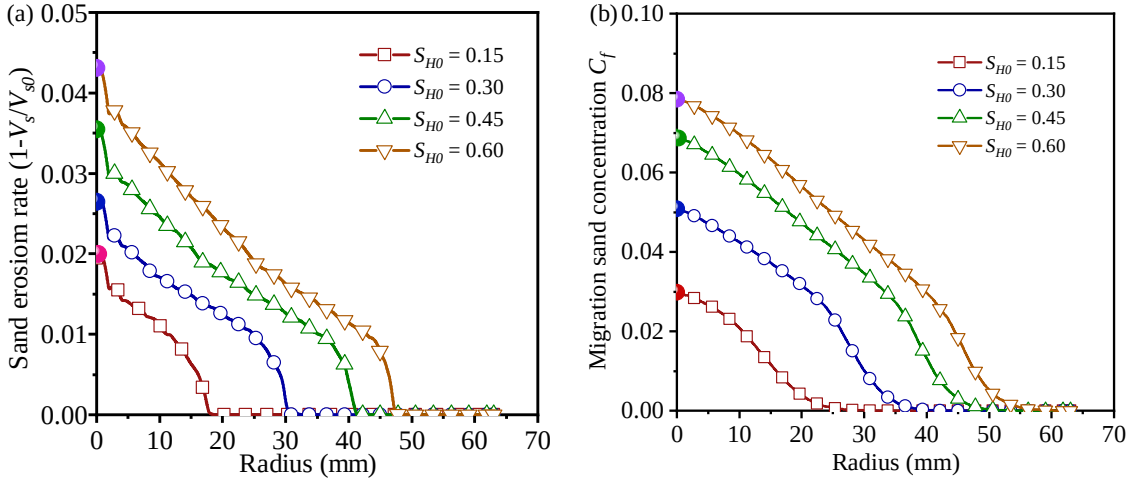

Fig. 16. Effect of hydrate saturation: (a) Sand erosion rate and (b) migration sand concentration.

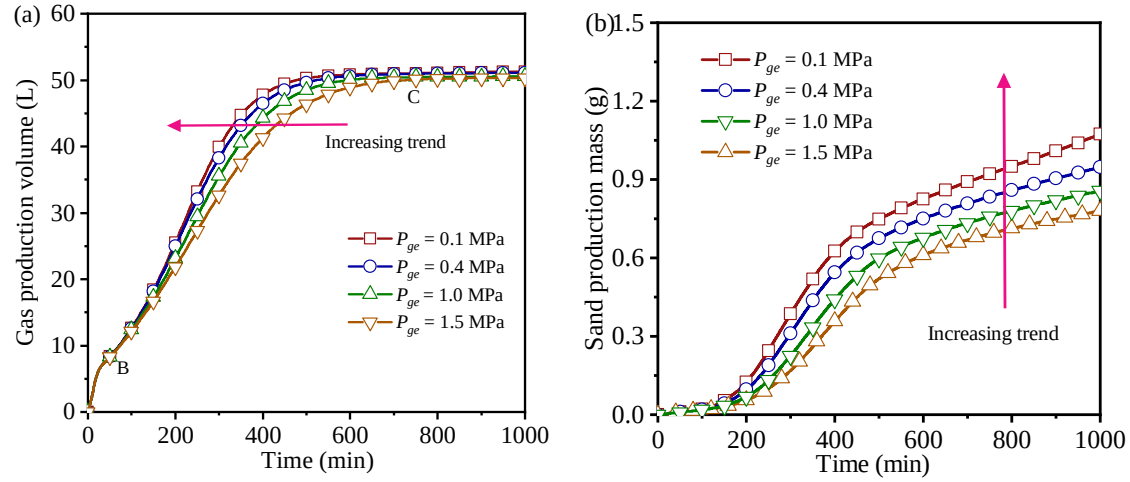

Fig. 17. Effect of depressurization pressure: (a) Gas production volume and (b) sand production mass.

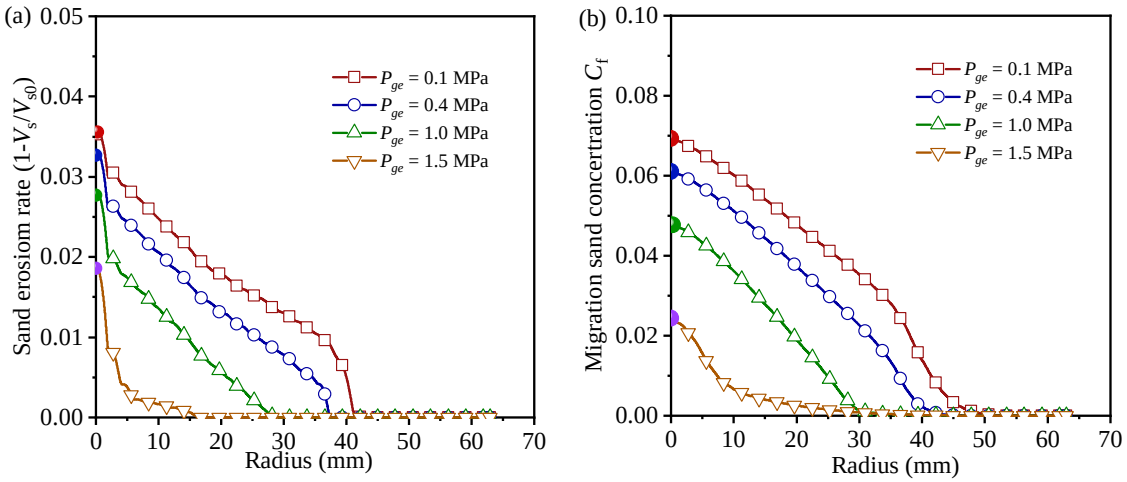

Fig. 18. Effect of depressurization pressure: (a) Sand erosion rate and (b) migration sand concentration.

The primary findings are summarized as follows:

1) The proposed model incorporates sand migration rate as an intrinsic component of the energy dissipation system, providing a unified theoretical framework that inherently captures the processes of hydrate dissociation and sand production.
2) Numerical implementation simulates the full cycle of sand erosion and migration driven by liquid seepage, mechanical deformation and hydrate dissociation. The Heaviside step function enables automatic switching between these phases, enhancing computational robustness.
3) Model validation encompasses dissociation tests both with and without considering sand migration. Hydrate dissociation and sand erosion progress more rapidly near the specimen edges, while they lag at the central region. The migration sand concentration first reaches a peak value and then begins to decline, while the sand erosion rate gradually increases and eventually stabilizes.

This study provides a valuable tool for predicting sand production risk induced by hydrate dissociation. The predictive performance of the model under extreme formation conditions and long-term production scenarios requires further validation.

Acknowledgements

The authors gratefully acknowledge the financial support provided by the National Natural Science Foundation of China (Nos. 52278327 and 52108296).

Conflicts of interest

The authors declare no competing interest.

References

Akaki, T., Kimoto, S. Numerical modelling of internal erosion during hydrate dissociation based on multiphase mixture theory. International Journal for Numerical and Analytical Methods in Geomechanics, 2020, 44(2): 327-350.

Bai, B., Wu, H., Zhou, R., et al. A granular thermodynamic framework-based coupled multiphase-substance flow model considering temperature driving effect. Journal of Rock Mechanics and Geotechnical Engineering, 2024, 17(9): 5816-5828.

Bai, B., Zhou, R., Yang, G., et al. The constitutive behavior and dissociation effect of hydrate-bearing sediment within a granular thermodynamic framework. Ocean Engineering, 2023, 268: 113408.

Cohen, E., Klar, A., Yamamoto, K. Micromechanical investigation of stress relaxation in gas hydrate-bearing sediments due to sand production. Energies, 2019, 12(11): 2131.

Cortis, A., Harter, T., Hou, L., et al. Transport of cryptosporidium parvum in porous media: Long-term elution experiments and continuous time random walk filtration modeling. Water Resources Research, 2006, 42(12): W12S13.

Dou, X., Liu, Z., Yang, D., et al. 3D CFD-DEM modeling of sand production and reservoir compaction in gas hydrate-bearing sediments with gravel packing well completion. Computers and Geotechnics, 2025, 177: 106870.

Fang, X., Ning, F., Wang, L., et al. Dynamic coupling responses and sand production behavior of gas hydrate-bearing sediments during depressurization: An experimental study. Journal of Petroleum Science and Engineering, 2021, 201: 108506.

Fuente, M., Vaunat, J., Marín-Moreno, H. Thermo-hydro-mechanical coupled modeling of methane hydrate-bearing sediments: Formulation and application. Energies, 2019, 12: 2178.

Fujisawa, K., Murakami, A., Nishimura, S. Numerical analysis of the erosion and the transport of fine particles within

soils leading to the piping phenomenon. Soils and Foundations, 2010, 50(4): 471-482.

Katagiri, J., Konno, Y., Yoneda, J., et al. Pore-scale modeling of flow in particle packs containing grain-coating and pore-filling hydrates: Verification of a Kozeny-Carman-based permeability reduction model. Journal of Natural Gas Science and Engineering, 2017, 45: 537-551.

Kazidenov, D., Omirbekov, S., Zhanabayeva, M., et al. Experimental and numerical study of the effect of polymer flooding on sand production in poorly consolidated porous media. Geoenergy Science and Engineering, 2025, 249: 213749.

Kimoto, S., Oka, F., Fushita, T. A chemo-thermo-mechanically coupled analysis of ground deformation induced by gas hydrate dissociation. International Journal of Mechanical Sciences, 2010, 52(2): 365-376.

Li, H., Hu, Q., Zhu, R. Reactive transport modeling of water-CO_2-rock interactions in clay-coated sandstones and implications for CO_2 storage. Advances in Geo-Energy Research, 2025, 17(2): 121-134.

Li, X., Wan, Y., Lei, G., et al. Numerical investigation of gas and sand production from hydrate-bearing sediments by incorporating sand migration based on IMPES method. Energy, 2024, 288: 129556.

Li, Y., Wang, L., Shen, S., et al. Triaxial tests on water-saturated gas hydrate-bearing fine-grained samples of the South China Sea under different drainage conditions. Energy & Fuels, 2021, 35(5): 4118-4126.

Li, Z., Yu, J., Wang, Y., et al. Experimental investigation on deformation of natural gas hydrate in the process of decompressing. Energy Procedia, 2019, 158: 5510-5516.

Lu, J., Xiong, Y., Li, D., et al. Experimental investigation of characteristics of sand production in wellbore during hydrate exploitation by the depressurization method. Energies, 2018, 11(7): 1673.

Murphy, A., Soga, K., Yamamoto, K. Experimental investigation into sand production from turbidite strata. Journal of Petroleum Science and Engineering, 2020, 190: 107056.

Ning, F., Fang, X., Liu, Z., et al. Sand production behaviors during gas recovery from sandy and clayey-silty hydrate-bearing sediments: A comparative analysis. Energy Science & Engineering, 2022, 10(7): 2224-2238.

Oyama, H., Nagao, J., Suzuki, K., et al. Experimental analysis of sand production from methane hydrate bearing sediments applying depressurization method. Journal of MMIJ, 2010, 126: 497-502.

Shen, J., Chiu, C., Ng, C., et al. A state-dependent critical state model for methane hydrate-bearing sand. Computers and Geotechnics, 2016, 75: 1-11.

Sibille, L., Marot, D., Sail, Y. A description of internal erosion by suffusion and induced settlements on cohesionless granular matter. Acta Geotechnica, 2015, 10(6): 735-748.

Sun, S., Gu, L., Tian, W., et al. Percolation characteristics of pore ffuid during hydrate depressurization dissociation from multi-phase multi-ffeld coupling analysis. Energy, 2023, 281: 128296.

Uchida, S., Seol, Y., Yamamoto, K. Sand migration simulation during gas production from gas hydrate reservoir at Kuparuk 7-11-12 site in the Prodhoe Bay Unit, Alaska. Energy & Fuels, 2022, 36(14): 7382-7390.

Wang, T., Wang, C., Zhang, F. Experimental study of fines migration in gap-graded soils with gas production: Implications to hydrate production from unconsolidated reservoirs. Geoenergy Science and Engineering, 2023, 227: 211856.

Wood, D., Maeda, K., Nukudani, E. Modelling mechanical consequences of erosion. Géotechnique, 2010, 6(60): 447-457.

Yang, J., Yin, Z., Laouafa, P. Modeling coupled erosion and filtration of fine particles in granular media. Acta Geotechnica, 2019, 14(6): 1615-1627.

Yoneda, J., Masui, A., Konno Y, et al. Mechanical properties of hydrate bearing turbidite reservoir in the first gas production test site of the Eastern Nankai Trough. Marine and Petroleum Geology, 2015, 66: 471-486.

Zhang, P., Gao, W., Ding, Y., et al. Mesoscale numerical investigation of fines detachment, migration, and erosion mechanisms in gas hydrate extraction. Acta Geotechnica, 2025, 20(10): 5469-5486.

Zhou, R., Bai, B., Chen, L., et al. A granular thermodynamic constitutive model considering THMC coupling effect for hydrate-bearing sediment. Ocean Engineering, 2024, 310: 118689.

Zhou, S., Chen, W., Li, Q., et al. Research on the solid fluidization well testing and production for shallow non-diagenetic natural gas hydrate in deep water area. China Offshore Oil and Gas, 2017, 29(04): 1-8. (in Chinese)

Zhu, H., Xu, T., Yuan, Y., et al. Numerical analysis of sand production during natural gas extraction from unconsolidated hydrate-bearing sediments. Journal of Natural Gas Science and Engineering, 2020, 76: 103229.